



## **ICQNM 2016**

The Tenth International Conference on Quantum, Nano/Bio, and Micro  
Technologies

ISBN: 978-1-61208-495-4

July 24 - 28, 2016

Nice, France

### **ICQNM 2016 Editors**

Victor Ovchinnikov, Aalto University, Finland

Thierry Ferrus, Hitachi Cambridge Laboratory, UK

# ICQNM 2016

## Forward

The Tenth International Conference on Quantum, Nano/Bio, and Micro Technologies (ICQNM 2016), held between July 24-28, 2016 in Nice, France, continued a series of events covering particularly promising theories and technologies. The conference covered fundamentals on designing, implementing, testing, validating and maintaining various kinds of materials, systems, techniques and mechanisms related to quantum-, nano- and micro-technologies.

We take here the opportunity to warmly thank all the members of the ICQNM 2016 technical program committee, as well as the reviewers. We also kindly thank all the authors that dedicated much of their time and effort to contribute to ICQNM 2016.

We also gratefully thank the members of the ICQNM 2016 organizing committee for their help in handling the logistics and for their work that made this professional meeting a success.

We hope ICQNM 2016 was a successful international forum for the exchange of ideas and results between academia and industry and to promote further progress in the area of Quantum, Nano/Bio, and Micro Technologies. We also hope that Nice, France provided a pleasant environment during the conference and everyone saved some time enjoy the beautiful French Riviera.

### **ICQNM 2016 Advisory Committee**

Vladimir Privman, Clarkson University - Potsdam, USA  
Christian Kollmitzer, AIT Austrian Institute of Technology GmbH, Austria  
Victor Ovchinnikov, Aalto University, Finland

### **ICQNM 2016 Research/Industry Chairs**

Marco Genovese, Italian Metrological Institute (INRIM) -Torino, Italy  
Keiji Matsumoto, National Institute of Informatics, Japan

### **ICQNM 2016 Special Area Chairs**

#### **QSEC**

Masahito Hayashi, Nagoya University, Japan

#### **Fluidics**

Alireza Azarbadegan, University College London (UCL), UK

#### **Quantum algorithms and quantum complexity**

Francois Le Gall, The University of Tokyo, Japan

#### **Quantum control**

Daoyi Dong, University of New South Wales, Australia

# ICQNM 2016

## Committee

### ICQNM Advisory Committee

Vladimir Privman, Clarkson University - Potsdam, USA  
Christian Kollmitzer, AIT Austrian Institute of Technology GmbH, Austria  
Victor Ovchinnikov, Aalto University, Finland

### ICQNM 2016 Research/Industry Chairs

Marco Genovese, Italian Metrological Institute (INRIM) -Torino, Italy  
Keiji Matsumoto, National Institute of Informatics, Japan

### ICQNM 2016 Special Area Chairs

#### QSEC

Masahito Hayashi, Nagoya University, Japan

#### Fluidics

Alireza Azarbadegan, University College London (UCL), UK

#### Quantum algorithms and quantum complexity

Francois Le Gall, The University of Tokyo, Japan

#### Quantum control

Daoyi Dong, University of New South Wales, Australia

### ICQNM 2016 Technical Program Committee

Andrew Adamatzky, University of the West of England - Bristol, U.K.  
Gerardo Adesso, University of Nottingham, UK  
Hossein Aghababa, University of Tehran, Iran  
Irina Buyanova, Linköping University, Sweden  
Weimin M. Chen, Linköping University, Sweden  
Taksu Cheon, Kochi University of Technology - Tosa Yamada, Japan  
Sang H. Choi, NASA Langley Research Center, USA  
Mihaela Corneanu, Banat's University of Agricultural Sciences and Veterinary Medicine, Romania  
Sorin Cotofana, TU Delft, The Netherlands  
Kamalika Datta, National Institute of Technology Meghalaya, Shillong, India  
Brahim Dennai, ENERGARID Laboratory, France  
Rolf Drechsler, University of Bremen/DFKI, Germany  
Sao-Ming Fei, Capital Normal University - Beijing, China  
Juan Carlos García-Escartín, Universidad de Valladolid, Spain

Yuval Gefen, The Weizmann Institute of Science, Israel  
Marco Genovese, Italian Metrological Institute (INRIM) -Torino, Italy  
Bonnie Gray, Simon Fraser University, Canada  
Masahito Hayashi, Nagoya University, Japan  
Hoshang Heydari, Stockholm University, Sweden  
Norman Hugh Redington, MIT, USA  
Chul Huh, Electronics and Telecommunications Research Institute (ETRI), Republic of Korea  
Travis Humble, Oak Ridge National Laboratory, USA  
Elżbieta Jankowska, National Research Institute - Warsaw, Poland  
Zhengfeng Ji, Institute for Quantum Computing - University of Waterloo, Canada  
Benjamin Jurke, Northeastern University - Boston, USA  
Alena Kalendova, Tomas Bata University in Zlin, Czech Republic  
Christian Kollmitzer, AIT Austrian Institute of Technology GmbH, Austria  
Francois Le Gall, The University of Tokyo, Japan  
Jun Li, Kansas State University, USA  
Gui Lu Long, Tsinghua University, China  
Stefano Mancini, University of Camerino, Italy  
Constantinos Mavroidis, Northeastern University - Boston, USA Munehiro Nishida, Hiroshima University, Japan  
Masaki Nakanishi, Yamagata University, Japan  
Andrej Orinak, University of P. J. Safarik in Kosice, Slovakia  
Victor Ovchinnikov, MICRONOVA, Aalto University, Finland  
Telhat Özdoğan, Amasya University, Turkey  
Bill Parker, CreativeMicro, USA  
Vladimir Privman, Clarkson University - Potsdam, USA  
Stefan Rass, Universität Klagenfurt, Austria  
Mohsen Razavi, University of Leeds, UK  
Philippe Renaud, Ecole Polytechnique Federale de Lausanne, Switzerland  
Luis Roa Oppliger, Universidad de Concepción, Chile  
Reza Sadr, Texas A&M University at Qatar – Doha, Qatar  
Barry Sanders, iCORE/University of Calgary, Canada  
Peter Schartner, University of Klagenfurt, Austria  
Stefan Schauer, AIT Austrian Institute of Technology GmbH, Austria  
Kristina Seklisinski, Université de Montréal, Canada  
Simone Severini, University College London, UK  
Ingo Sieber, Karlsruher Institut für Technologie (KIT), Germany  
Anuvat Sirivat, Chulalongkorn University, Thailand  
Maciej Sitarz, AGH University of Science and Technology - Cracow, Poland  
Don Sofge, Naval Research Laboratory - Washington D.C., USA  
Sandro Sozzo, School of Management and Institute for Quantum Social and Cognitive Science - University of Leicester, UK  
Ashok Srivastava, Louisiana State University, Baton Rouge, USA  
Eric Suraud, Université Paul Sabatier, France  
Alexander Tarasenko, Institute of Physics Academy of Sciences of the Czech Republic, Czech Republic  
Tzyh Jong Tarn, Washington University in St. Louis, USA and Tsinghua University - Beijing, China  
Pramod Tiwari, National Institute of Technology - Rourkela - Odisha, India  
Adriana Vâlcu, National Institute of Metrology, Romania  
Salvador E. Venegas-Andraca, Tecnológico de Monterrey, Mexico

Robert Wille, Johannes Kepler University Linz, Austria

Shigeru Yamashita, Ritsumeikan University - Shiga Japan

Katerina Zaharieva, Institute of Catalysis - Bulgarian Academy of Sciences, Bulgaria

Alexander Zhanov, Gwangju Institute of Science and Technology (GIST), Republic of Korea

## Copyright Information

For your reference, this is the text governing the copyright release for material published by IARIA.

The copyright release is a transfer of publication rights, which allows IARIA and its partners to drive the dissemination of the published material. This allows IARIA to give articles increased visibility via distribution, inclusion in libraries, and arrangements for submission to indexes.

I, the undersigned, declare that the article is original, and that I represent the authors of this article in the copyright release matters. If this work has been done as work-for-hire, I have obtained all necessary clearances to execute a copyright release. I hereby irrevocably transfer exclusive copyright for this material to IARIA. I give IARIA permission to reproduce the work in any media format such as, but not limited to, print, digital, or electronic. I give IARIA permission to distribute the materials without restriction to any institutions or individuals. I give IARIA permission to submit the work for inclusion in article repositories as IARIA sees fit.

I, the undersigned, declare that to the best of my knowledge, the article does not contain libelous or otherwise unlawful contents or invading the right of privacy or infringing on a proprietary right.

Following the copyright release, any circulated version of the article must bear the copyright notice and any header and footer information that IARIA applies to the published article.

IARIA grants royalty-free permission to the authors to disseminate the work, under the above provisions, for any academic, commercial, or industrial use. IARIA grants royalty-free permission to any individuals or institutions to make the article available electronically, online, or in print.

IARIA acknowledges that rights to any algorithm, process, procedure, apparatus, or articles of manufacture remain with the authors and their employers.

I, the undersigned, understand that IARIA will not be liable, in contract, tort (including, without limitation, negligence), pre-contract or other representations (other than fraudulent misrepresentations) or otherwise in connection with the publication of my work.

Exception to the above is made for work-for-hire performed while employed by the government. In that case, copyright to the material remains with the said government. The rightful owners (authors and government entity) grant unlimited and unrestricted permission to IARIA, IARIA's contractors, and IARIA's partners to further distribute the work.

## Table of Contents

Population Inversion by an Adiabatic Cycle in 1D Boson System <i>Taksu Cheon and Atushi Tanaka</i>	1
Reduction of Silver Oxide Film in Inert Gas Plasma <i>Victor Ovchinnikov</i>	6
Quantum Hexagonal Quadrature Amplitude Modulation <i>YoungJun Kim and Young-Chai Ko</i>	12
The Formation of Black Glasses from Ladder-like Silsequioxanes <i>Maciej Sitarz</i>	17

# Population Inversion by an Adiabatic Cycle in 1D Boson System

Taksu Cheon

Laboratory of Physics, Kochi University of Technology  
 Tosa Yamada, Kochi 782-8502, Japan  
 Email: taksu.cheon@kochi-tech.ac.jp

Atushi Tanaka

Department of Physics, Tokyo Metropolitan University  
 Hachioji, Tokyo 192-0397, Japan  
 Email: tanaka-atushi@tmu.ac.jp

**Abstract**—In this paper, we show that an adiabatic cycle excites Bose particles confined in a one-dimensional box. We consider a cycle, during which a wall described by a  $\delta$ -shaped potential is applied and its strength and position are slowly varied. When the system is initially prepared in the equilibrium ground state, the adiabatic cycle brings all bosons into the first excited one-particle state, leaving the system in a nonequilibrium state. The absorbed energy during the cycle is proportional to the number of bosons.

**Keywords**—Quantum mechanics; Quantum holonomy; Ultracold gases.

## I. INTRODUCTION

The control of a physical system in at quantum level is at the forefront of today's physics research. Among the research works, the population inversion in bosonic gas has a venerable tradition, dating back to the early years of quantum mechanics. The quantum population inversion has been studied for its application to lasing [1]. The quantum control of atoms and molecules has also been investigated to realize the population inversion [2][3]. Recently, studies of the super-Tonks-Girardeau gas, which also involves the population inversion, have attracted a lot of attention in both experimental and theoretical studies of nonequilibrium cold atoms [4][5][6][7]. In the super-Tonks-Girardeau gas, which may be described by the Lieb-Liniger model [8] with strongly attractive interaction, the population inversion is created through an "adiabatic" process, where the interaction strength is suddenly flipped from infinitely repulsive to infinitely attractive [6][9].

Such a population inversion can be induced even by an adiabatic cycle, which can be obtained with an extension of the adiabatic process that connects Tonks-Girardeau and super-Tonks-Girardeau gases both to weaker repulsive and weaker attractive regime. The repetitions of this adiabatic cycle transform the ground state of non-interacting bosons into their higher excited states and achieve the population inversion [10]. This is counterintuitive, since there is no external field to drive the final state of the bosons away from the initial state.

There have been studies of the excitation of quantum systems by adiabatic cycles, which is referred to as the exotic quantum holonomy [11][12][13]. We also mention, in studies of atomic and molecular systems under the oscillating field, that an adiabatic cycle involving a level crossing may excite a quantum system [14][15].

In this paper, we examine an adiabatic cycle that excites a system consisting of Bose particles confined in a one-dimensional box. During the cycle, we vary an additional wall adiabatically, while the interparticle interaction is kept fixed.

This is in contrast to the scheme described in [6][10], where the interaction strength between Bose particles is an effective adiabatic parameter. In this study, we suppose that the wall is described by a  $\delta$ -function shaped potential [16][17][18]. We show that the first excited one-particle state is occupied by all the bosons to achieve the population inversion completely, if the system is prepared to be in the ground state. Namely, the energy gained by the bosons during the adiabatic cycle is proportional to the number of bosons.

The paper is organized as follows. In section 2, the basic setup of our model is presented in the simplest setting of one boson. Section 3 and 4 deal with noninteracting and interacting many bosons, respectively. The summary and the discussion are found in Section 5.

## II. A PARTICLE IN A BOX WITH A $\delta$ -WALL

In order to examine  $N$  Bose particles in a one-dimensional box with an additional  $\delta$ -wall, we review the single particle case, i.e.,  $N = 1$  [18], where the system is described by the Hamiltonian

$$H(g, X) = \frac{p^2}{2m} + V(x) + g\delta(x - X), \quad (1)$$

where  $m$  is the particle mass,  $V(x)$  is the confinement potential, and  $g$  and  $X$  are the strength and position of  $\delta$ -wall. In particular, we assume that  $V(x)$  describes an infinite square well with the length  $L$ , i.e.,  $V(x) = 0$  for  $0 < x < L$  and  $V(x) = \infty$  otherwise [16][17].

We introduce an adiabatic cycle  $C$ , which consists of three adiabatic processes  $C_I$ ,  $C_{II}$  and  $C_{III}$ , as shown in Figure 1. We suppose that the  $\delta$ -wall is initially absent, i.e.,  $g = 0$  in 1, and that the system is in a stationary state initially. In the first part of  $C$ , which will be called  $C_I$ , an impenetrable wall is inserted at  $x_0$  adiabatically. In terms of the  $\delta$ -wall, the strength  $g$  is slowly increased from 0 to  $\infty$ , while its position  $X$  is fixed at  $x_0$  during  $C_I$ . Subsequently, in the second part  $C_{II}$ , the position  $X$  of the impenetrable wall is adiabatically changed

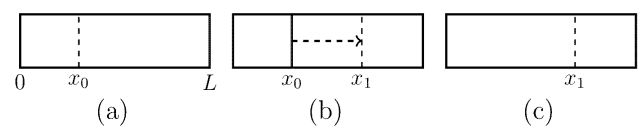


Figure 1. The adiabatic cycle  $C$  of a one-dimensional box, which contains Bose particles. The strength and the position of an additional  $\delta$ -wall is adiabatically varied during  $C$ .

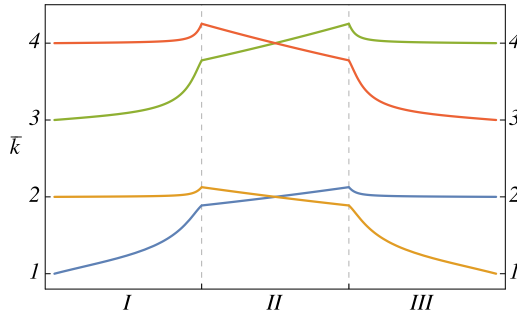


Figure 2. Parametric evolution of eigenenergies with  $N = 1$  along the cycle  $C$ , which consists of  $C_I$  (left part),  $C_{II}$  (middle part) and  $C_{III}$  (right part). The eigenenergies are depicted by their normalized wavenumber  $\bar{k}$  2. We set  $x_0 = 0.4703L$  and  $x_1 = L - x_0$ .

from  $x_0$  to  $x_1$ . In the last part  $C_{III}$ , the  $\delta$ -wall at  $X = x_1$  is adiabatically turned off. At the end of the cycle  $C$ , the  $\delta$ -wall has no effect, again.

In Figure 2, we depict the parametric dependence of eigenenergies of the single-particle Hamiltonian  $H(g, X)$  1 along  $C$ . Throughout this manuscript, we indicate the eigenenergy  $E$  using a normalized wavenumber  $\bar{k}$

$$\bar{k} \equiv \sqrt{\frac{E}{N\epsilon}}, \quad (2)$$

where  $\epsilon = (\hbar\pi/L)^2/(2m)$  is the ground eigenenergy of the particle in the infinite square well.

The adiabatic time evolution of the single-particle system along  $C$  depends on  $x_0$  and  $x_1$ . In the following, we explain the case  $\frac{2}{5}L < x_0 < \frac{1}{2}L < x_1 < \frac{3}{5}L$ , which may be explained from Figure 2. A more rigorous argument is found in [18].

First, let us consider the case that the initial state is the ground state  $|1(g = 0, X = x_0)\rangle$  of the particle in the infinite square well, where  $|n(g, X)\rangle$  denotes the  $n$ -th adiabatic eigenstate of  $H(g, X)$  during processes  $C_I$  and  $C_{III}$ . We will omit to indicate  $(g, X)$  in the following. After the completion of  $C_I$ , the state vector arrives at  $|R_1\rangle$ , the ground state of the right well, since we choose the right well in  $C_{II}$  is slightly larger than the left well. During  $C_{II}$ , there occurs a spectral degeneracy between  $|R_1\rangle$  and  $|L_1\rangle$ , the ground state of the left well. This is because the size of the left (right) well is increasing (decreasing) during  $C_{II}$ , and these sizes coincide at  $X = L/2$ . At the end of  $C_{II}$ ,  $|R_1\rangle$  becomes the first excited state, which adiabatically continued to  $|2\rangle$ , which is the second excited state of the particle in the infinite square well, through  $C_{III}$ . Hence, the ‘‘population inversion’’ in the single-particle system occurs if the system is prepared to be in the ground state initially.

Second, we examine the case that the initial state is the first excited state  $|2\rangle$ , which offers the ‘‘inverse’’ of the population inversion. Through the adiabatic cycle  $C$ , the system arrives at  $|L_1\rangle$  after the completion of  $C_I$ , and then arrives at  $|1\rangle$  at the end of the cycle  $C$ . Namely, either  $|1\rangle$  and  $|2\rangle$  return to the initial states after the completion of the adiabatic cycle  $C$  twice.

Third, let us examine the cases that the initial states are  $|3\rangle$  and  $|4\rangle$ , which are the first and second excited state, respectively. Now  $C$  induces an interchange of these two

states, through the intermediate states  $|R_2\rangle$  and  $|L_2\rangle$ , which are localized the right and left well during the process II.

A similar interchange of initial eigenstates occurs as a result of the adiabatic cycle  $C$ , as long as we choose  $x_0$  and  $x_1$  appropriately. In general, the level crossing of the one-particle Hamiltonian 1 during the process  $C_{II}$  plays an important role to determine which pairs of eigenstates are interchanged by  $C$ , while there is no level crossing generically during the processes  $C_I$  and  $C_{III}$  [18].

We make a remark on the stability of the present scheme for the one-body population inversion. A crucial point is the stability of the adiabatic time evolution across the level crossing during  $C_{II}$ . The level crossing may be lifted due to an imperfection of the impenetrable wall, i.e., the  $\delta$ -wall with an infinite strength. If the level splitting is small enough, we may employ the diabatic process around the avoided crossing to realize the one-body population inversion. It has been shown that an open diabatic process made of time-dependent potential well produces the second excited state from the ground state of a bose particle [19]. This diabatic scheme is applied to create collective excitations of interacting bosons [19][20][21].

### III. NON-INTERACTING BOSONS

We examine the case that the number of the Bose particles is  $N$ , assuming the absence of interparticle interaction. It is straightforward to extend the above result for  $N = 1$ , once we restrict the case that  $N$  bosons initially occupy the one-particle state  $|n\rangle$ . Hence, the system is in an adiabatic state of the  $N$  bosons

$$|n^{\otimes N}\rangle \equiv |nn\dots n\rangle, \quad (3)$$

where the one-particle adiabatic state  $|n\rangle$  is occupied by  $N$  bosons, during  $C_I$  and  $C_{III}$ .

If there are no interparticle interactions, the parametric evolution of averaged wavenumber  $\bar{k}$  for the adiabatic  $N$ -particle state agrees with the one of the single-particle system. This suggests that the adiabatic cycle  $C$  of the  $N$ -particle system with no interaction delivers the ground state  $|1^{\otimes N}\rangle$  to the excited state  $|2^{\otimes N}\rangle$ , i.e., the complete population inversion, as seen in Figure 2. The energy that the particles acquire during the cycle  $C$  is proportional to the number of the particles.

### IV. INTERACTING BOSONS

We examine the adiabatic cycle  $C$  for  $N$  interacting Bose particles. We mainly examine the case that the system is initially in the ground state. In order to confirm that the  $N$ -particle population inversion really occurs, we need to examine the effect of the interparticle interaction.

We assume that the interparticle interaction  $V$  consists of two-body contact interactions. Namely, we suppose that  $V$  takes the following form

$$V(x_1, x_2, \dots, x_N) = \lambda \sum_{\langle i, j \rangle} \delta(x_i - x_j), \quad (4)$$

where  $\lambda$  is the interaction strength, and the summation is taken over pairs.

We also assume that the interparticle interaction is weak enough so that the topology of the parametric dependence of eigenenergy remains unchanged, except around the level crossing points of the noninteracting bosons. Namely, when

the gaps of the eigenenergies between neighboring levels in the noninteracting system are larger than a constant value, the interparticle interaction shifts the eigenenergy at most  $\mathcal{O}(\lambda)$ , according to the standard perturbation theory. For small enough perturbative energy correction, the corresponding adiabatic time evolution of the stationary state of the interacting bosons closely follows the one of the noninteracting bosons.

Accordingly, under the weak interparticle interaction condition, the eigenstates of the interacting bosons can be labeled by the quantum numbers of the noninteracting bosons. For example, the ground state of the initial and final points of the adiabatic cycle  $C$  may be denoted as  $|1^{\otimes N}(\lambda)\rangle$ , whose overlapping integral with the unperturbed state  $|1^{\otimes N}\rangle$  is large. Also,  $|1^{\otimes N}(\lambda)\rangle$  can be constructed by the standard perturbation theory with a small parameter  $\lambda$ .

On the other hand, even a weak interparticle interaction can strongly influence the parametric evolution of energy levels in the vicinity of level crossings by making avoided crossings. Hence, we need to closely examine the level crossing of the non-interacting Bose particles.

In the following, we argue that the adiabatic time evolution closely follows the one in the noninteracting system examined above, if the number of particles is large enough. The key is the selection rule for the matrix element of  $V$  in the adiabatic representation in the vicinity of the level crossings of non-interacting Bosons.

#### A. "Tunneling" and direct contributions of the interaction in $N = 2$

We show that the effect of the interparticle interaction is significantly different, depending on whether a level crossing locates either in  $C_{II}$ , or in  $C_I \cup C_{III}$ , as for the two body case. In the former case, the relevant matrix elements may be small since it involves only tunneling processes through the impenetrable wall. On the other hand, in processes  $C_I$  and  $C_{III}$ , the matrix element cannot be negligible. However, it turns out that there happens to be no corresponding level crossing that affects the population inversion whose initial state is the ground state.

The parametric evolutions of eigenenergies of the noninteracting two particle system are depicted in Figure 3, in terms of the averaged wavenumber  $\bar{k}$  (see, 2). The parametric evolution of the eigenenergy that connects  $|11\rangle$  and  $|22\rangle$  has a level crossing with two eigenenergies during  $C_{II}$ . The initial states of these energy levels are  $|22\rangle$  and  $|12\rangle$ , which are  $|L_1L_1\rangle$  and  $|R_1L_1\rangle$  during  $C_{II}$ , respectively.

We examine the matrix elements of the interparticle interaction term  $V$  between the adiabatic basis vectors  $|R_1R_1\rangle$ ,  $|L_1L_1\rangle$  and  $|R_1L_1\rangle$ . Note that  $|R_1R_1\rangle$  corresponds to the initial state  $|11\rangle$  of the adiabatic cycle

$$\langle R_1, L_1 | V | R_1, R_1 \rangle = \sqrt{2}\lambda \int_0^L \{\psi_{R_1}(x)\psi_{L_1}(x)\}^* \{\psi_{R_1}(x)\}^2 dx, \quad (5)$$

for example. Since the single-particle adiabatic eigenfunctions  $\psi_{L_1}(x)$  and  $\psi_{R_1}(x)$  are completely localized in the left and right wells, respectively, the overlapping integral is zero, if the  $\delta$ -wall is completely impenetrable during  $C_{II}$ . The level crossing accordingly remains even in the presence of the interparticle interaction. Thus the adiabatic cycle  $C$  induces

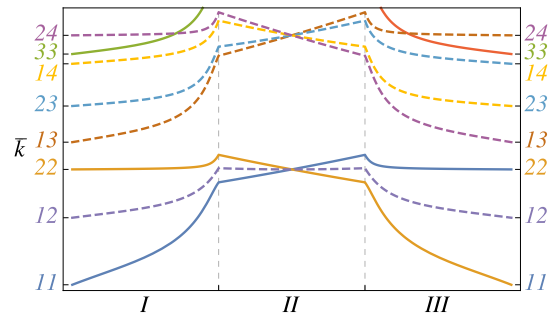


Figure 3. Parametric evolution of normalized wavenumbers for  $N = 2$ . Full lines indicate the levels whose initial states are  $|nn\rangle$  ( $n = 1, \dots, 4$ ). Other levels are depicted by dashed lines. Parameters are the same as in Figure 2.

the complete population inversion from  $|11\rangle$  to  $|22\rangle$ , as in the non-interacting case.

Let us examine the case that the  $\delta$ -wall during  $C_{II}$  allows the tunneling leakage of particles due to some imperfections. Still, we may expect that the matrix elements due to the tunneling corrections are exponentially small. Since the resultant energy gap of the avoided crossing is also exponentially small, we may expect that the diabatic process easily almost recovers the complete population inversion.

Also, during the second process  $C_{II}$ , the left and right part of the well may be separated. This allows us to make the tunneling correction arbitrarily small. Accordingly the adiabatic limit that follows the extremely small avoided crossing would be difficult to realize.

On the other hand, if the level crossing appears during  $C_I$  or  $C_{III}$ , the interparticle interaction destroys the level crossing. In Figure 3, such an example is seen between the levels whose initial states are  $|33\rangle$  and  $|24\rangle$ , which is delivered to  $|R_2R_2\rangle$  and  $|L_1L_2\rangle$ , respectively, in the absence of  $V$ .

The matrix element  $\langle 33 | V | 24 \rangle$  does not vanish in general, since the relevant single-particle adiabatic eigenfunctions extend the whole box. Accordingly the level crossings are destroyed to form avoided crossing. Thus the adiabatic process  $C_I$  for example, delivers  $|33\rangle$  and  $|24\rangle$  at the initial point of  $C_I$ , to  $|L_1L_2\rangle$  and  $|R_2R_2\rangle$ , respectively. This breaks the population inversion whose initial state is a higher excited state, e.g., the adiabatic cycle  $C$  delivers  $|33\rangle$  to  $|44\rangle$  in the absence of the interparticle interaction.

#### B. Selection rule for $N = 3$

Here, we show that the interparticle interaction does not suppress the population inversion for  $N > 2$  due to a selection rule of  $V$ .

We explain this with the case  $N = 3$  (Figure 4). Let us examine the level whose initial state is  $|1^{\otimes 3}\rangle$  along  $C$ . The corresponding final state is  $|2^{\otimes 3}\rangle$  in the absence of the interparticle interaction.

First, the interparticle interaction has no, or exponentially small effect on the level crossing during  $C_{II}$ , as shown in the case of  $N = 2$ .

Second, we examine the level crossing in  $C_{III}$ , where the levels whose final states are  $|2^{\otimes 3}\rangle$  and  $|113\rangle$  exhibit crossing. We examine the matrix element of the interparticle

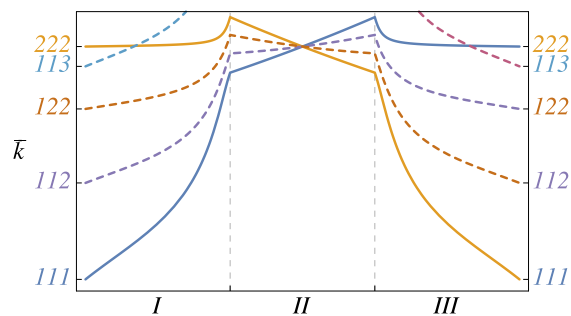


Figure 4. Parametric evolution of normalized wavenumbers for  $N = 3$ . Other parameters are the same as in Figure 3.

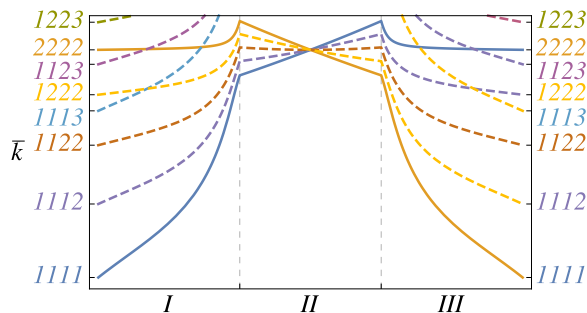


Figure 5. Parametric evolution of normalized wavenumbers for  $N = 4$ . Other parameters are the same as in Figure 3.

interaction  $\langle 113|V|2^{\otimes 3}\rangle$ , which vanishes since  $V$  is a two-body interaction, and the set of quantum numbers  $(1, 1, 3)$  and  $(2, 2, 2)$  has no common quantum number.

Still, there may be a tiny avoided crossing whose magnitude can be explained by the standard second-order perturbation theory. We may expect that the diabatic process induces the complete population inversion whose final state is  $|2^{\otimes 3}\rangle$ . Also, even if the interaction strength  $\lambda$  is moderately large, where the topology of the level diagram remains unchanged except that the avoided crossing becomes noticeable, the final state should be  $|113\rangle$ , whose energy is far larger than the ground state. In this sense, a incomplete population inversion should be realized.

### C. The population inversion for $N > 2$

We shall prove that the adiabatic cycle  $C$  delivers  $|1^{\otimes N}\rangle$  to  $|2^{\otimes N}\rangle$  for  $N > 2$ , even in the presence of the two-body interparticle interaction. Here we explain the selection rule for arbitrary  $N (> 2)$ , and examine each part of the cycle  $C$ . For example,  $N = 4$  case is shown in Figure 5.

We explain the selection rule of the two-body interparticle interaction for  $N > 2$ . Namely, we examine the matrix element  $\langle n'_1 n'_2 \dots n'_N | V | n_1 n_2 \dots n_N \rangle$ . The matrix element vanishes when the two sets of quantum numbers  $(n'_1, n'_2, \dots, n'_N)$  and  $(n_1, n_2, \dots, n_N)$  has, at least, three different elements, i.e., the number of the common quantum numbers is equal to  $N - 3$  or less. In other words, non-vanishing matrix element has the following  $\langle n'_1 n'_2 n'_3 \dots n'_N | V | n_1 n_2 n_3 \dots n_N \rangle$  where  $(n_3, \dots, n_N)$  are the common quantum numbers.

We examine the first part  $C_I$  of  $C$ . We assume that the system is initially in the ground state  $|1^{\otimes N}(\lambda)\rangle$ . According to the selection rule, it is sufficient to examine  $|1^{\otimes N-2}\psi, \phi\rangle$ , where  $|\psi\rangle$  and  $|\phi\rangle$  are single particle adiabatic states, e.g.  $|2\rangle$ . Now we examine whether the eigenenergies of these states are degenerate. This is equivalent to compare the eigenenergies corresponding to  $|11\rangle$  and  $|\psi, \phi\rangle$  of the two particle system. As is seen in Figure 3, there is no level crossing in  $C_I$ . In this sense, there is no effective level crossing with the level  $|1^{\otimes N}(\lambda)\rangle$ , during  $C_I$ .

As for  $C_{III}$ , we conclude from an argument similar to the above, that the energy level corresponding to  $|2^{\otimes N}(\lambda)\rangle$  has no effective level crossing.

Next we examine  $C_{II}$ , where the system is in  $|R_1^{\otimes N}\rangle$ . According to the selection rule, it suffices to examine  $|R_1^{\otimes N-2}\psi, \phi\rangle$  with single particle adiabatic states  $|\psi\rangle$  and  $|\phi\rangle$ . To clarify the level crossing, we compare  $|R_1 R_1\rangle$  with  $|\psi, \phi\rangle$ . There are three cases. First, the levels corresponding to  $|R_1 R_1\rangle$  and  $|R_n, R_{n'}\rangle$  ( $(n, n') \neq (1, 1)$ ) do not occur. Second, the levels corresponding to  $|R_1 R_1\rangle$  and  $|R_n, L_{n'}\rangle$  exhibits a degeneracy only when  $n = 1$  and  $n' = 1$ , where the corresponding matrix element involves a single-particle tunneling. Third, the levels corresponding to  $|R_1 R_1\rangle$  and  $|L_n, L_{n'}\rangle$  exhibits a degeneracy only when  $n = 1$  and  $n' = 1$ , where the corresponding matrix element involves a two-particle tunneling. Since the matrix elements involving a tunneling contribution is exponentially small, the resultant gap should be also small. Hence, the diabatic process should occur even when the speed of the impenetrable wall is moderately slow.

## V. DISCUSSION AND SUMMARY

We argue here that the experimental realization of the population inversion suggested in this paper is feasible with the current state of the art. For example, we may utilize the scheme [22] to realize  $\delta$ -wall with an approximate Gaussian wall.

Another possibility is to use a heavy particle as a wall, whose position may be manipulated by, say, an optical tweezer. The effective interaction between the wall particle and other particle may be tuned by external fields.

We note that the present scheme may offer a way to realize other exotic nonequilibrium states. Let us suppose, for example, the state of bosons is in  $|2^{\otimes N}(\lambda)\rangle$ , which can be generated from the adiabatic cycle  $C$ . After the interparticle interaction  $\lambda$  is adiabatically increased to  $\infty$ , the system arrives the higher excited state of the Tonks-Girardeau system, which may be described by the Lieb-Linigher model with the infinite interparticle interaction strength [23][24]. Similarly, after  $\lambda$  is adiabatically decreased to  $-\infty$ , the system now arrives at the higher excited state of the super-Tonks-Girardeau system [6]. This state is a much more highly-excited state compared to the super-Tonks-Girardeau state, because the initial state  $|2^{\otimes N}(\lambda)\rangle$  is a higher excited state of noninteracting bosons.

In summary, we have shown that the adiabatic cycle  $C$  induces the nearly complete population inversion of the multi-boson system, when the interparticle interaction is not too strong. As pointed out in [18] for a single particle case, the present scheme may be extended to the case of an arbitrary shape of the confinement potential  $V(x)$ .

ACKNOWLEDGEMENTS

This research was supported by the Japan Ministry of Education, Culture, Sports, Science and Technology under the Grant number 15K05216.

- [24] T. Kinoshita, T. Wenger and D. S. Weiss, "Observation of a One-Dimensional Tonks-Girardeau Gas", *Science* 305, pp. 1125–1128, 2004.

REFERENCES

- [1] G. Grynberg, A. Aspect and C. Fabre, *Introduction to Quantum Optics* (Cambridge: Cambridge University Press) 2010.
- [2] B. W. Shore, *Manipulating Quantum Structures Using Laser Pulses* (Cambridge: Cambridge University Press) 2011.
- [3] M. Shapiro and P. Brumer, *Quantum Control of Molecular Processes* 2nd ed (Weinheim: Wiley) 2012.
- [4] G. E. Astrakharchik, J. Boronat, J. Casulleras and S. Giorgini, "Beyond the Tonks-Girardeau Gas: Strongly Correlated Regime in Quasi-One-Dimensional Bose Gases", *Phys. Rev. Lett.* 95, 190407 (4pp), 2005.
- [5] M. Olshanii, "Atomic Scattering in the Presence of an External Confinement and a Gas of Impenetrable Bosons", *Phys. Rev. Lett.* 81, pp. 938–941, 1998.
- [6] E. Haller, M. Gustavsson, M. J. Mark, J. G. Danzl, R. Hart, G. Pupillo and H. C. Nägerl, "Realization of an Excited, Strongly Correlated Quantum Gas Phase", *Science* 325, pp. 1224–1227, 2009.
- [7] X. Guan, "Critical Phenomena in One Dimension from a Bethe Ansatz Perspective", *Int. J. Mod. Phys. B* 28, 1430015 (39pp), 2014.
- [8] E. H. Lieb and W. Liniger, "Exact Analysis of an Interacting Bose Gas. I. The General Solution and the Ground State", *Phys. Rev.* 130 pp. 1605–1616, 1963.
- [9] M. Girardeau, "Relationship between Systems of Impenetrable Bosons and Fermions in One Dimension", *J. Math. Phys.* 1, pp. 516–523, 1960.
- [10] N. Yonezawa, A. Tanaka and T. Cheon, "Quantum Holonomy in the Lieb-Liniger Model", *Phys. Rev. A* 87, 062113 (6pp), 2013.
- [11] T. Cheon, "Double Spiral Energy Surface in One-dimensional Quantum Mechanics of Generalized Pointlike Potentials", *Phys. Lett. A* 248, pp. 285–289, 1998.
- [12] A. Tanaka and M. Miyamoto, "Quasienergy Anholonomy and its Application to Adiabatic Quantum State Manipulation", *Phys. Rev. Lett.* 98, 160407 (4pp), 2007.
- [13] A. Tanaka and T. Cheon, "Bloch Vector, Disclination and Exotic Quantum Holonomy", *Phys. Lett. A* 379, pp.1693–1698, 2015.
- [14] N. V. Vitanov, T. Halfmann, B. W. Shore and K. Bergmann, "Laser-induced Population Transfer by Adiabatic Passage Techniques", *Annu. Rev. Phys. Chem.* 52, 763-809, 2001.
- [15] S. Guérin, L. P. Yatsenko and H. R. Jauslin, "Dynamical Resonances and the Topology of the Multiphoton Adiabatic Passage", *Phys. Rev. A* 63, 031403(R) (4pp), 2001.
- [16] S. Flügge, *Practical Quantum Mechanics* vol 1 (Berlin: Springer-Verlag) 1971.
- [17] A. G. Ushveridze, "Analytic Properties of Energy Levels in Models with Delta-function Potentials", *J. Phys. A* 21, pp. 955–970, 1988.
- [18] S. Kasumie, M. Miyamoto and A. Tanaka, "Adiabatic Excitation of a Confined Particle in One Dimension with a Variable Infinitely Sharp Wall", *Phys. Rev. A* 93, 042105 (5pp), 2016.
- [19] Z. P. Karkuszewski, K. Sacha and J. Zakrzewski, "Method for Collective Excitation of a Bose-Einstein Condensate", *Phys. Rev. A* 63, 061601(R) (4pp), 2001.
- [20] B. Damski, Z. P. Karkuszewski, K. Sacha and J. Zakrzewski, "Simple Method for Excitation of a Bose-Einstein Condensate", *Phys. Rev. A* 65, 013604 (7pp), 2002.
- [21] Z. P. Karkuszewski, K. Sacha and A. Smerzi, "Mean Field Loops versus Quantum Anti-crossing Nets in Trapped Bose-Einstein Condensates", *Eur. Phys. J. D* 21, pp. 251–254, 2002.
- [22] T. P. Meyrath, F. Schreck, J. L. Hanssen, C. S. Chuu and M. G. Raizen, "Bose-Einstein Condensate in a Box", *Phys. Rev. A* 71, 041604(R) (4pp), 2005.
- [23] B. Paredes, A. Widera, V. Murg, O. Mandel, S. Fölling, I. Cirac, G. V. Shlyapnikov, T. W. Hansch, I. and Bloch, "Tonks-Girardeau Gas of Ultracold Atoms in an Optical Lattice", *Nature* 499, pp. 277–281, 2004.

# Reduction of Silver Oxide Film in Inert Gas Plasma

Victor Ovchinnikov

Department of Aalto Nanofab

School of Electrical Engineering, Aalto University

Espoo, Finland

e-mail: Victor.Ovchinnikov@aalto.fi

**Abstract**— Reduction of silver oxide in plasma is studied. Silver oxide film was prepared by plasma oxidation of thermally evaporated silver film. It is shown that silver oxide is reduced with different rate in He, Ar and N<sub>2</sub> plasmas excited by rf power. To clarify mechanism of reduction, morphology, electrical and optical properties of the samples are analyzed. Spectroscopic ellipsometry is used to measure thicknesses and optical constants of oxidized and reduced layers. It is concluded that the reduction is activated by low energy electron bombardment of silver oxide.

**Keywords**-silver oxide; plasma reduction; silver thin film.

## I. INTRODUCTION

Both silver and silver oxide are widely used as functional material in microdevices. Silver is the best plasmonic material in visible range and has found broad application in sensors, photonics, catalysis and spectroscopy [1]. Unique properties of silver oxide are used in optical storage devices, gas sensors, photovoltaic cells and photonics [2]. Silver and silver oxide are applied both in the form of thin films, and in the form of nanostructures. Additionally, non-stoichiometric silver oxide Ag<sub>x</sub>O or silver oxide with silver inclusions can be used instead of pure oxide. Properties of silver oxide nanostructures and thin films are found to be sensitive to fabrication method. It has caused a big variety of the applied methods, such as thermal evaporation [3], reactive magnetron sputtering [4], chemical-bath deposition [5], exposing silver films to atomic oxygen environment [6][7], and so on. The last method is very attractive, because it opens an opportunity for application of well known Ag deposition methods in preparation of silver oxide films. Furthermore, interconversion of Ag into Ag<sub>x</sub>O and Ag<sub>x</sub>O in Ag would be desirable for fabrication of silver containing nanostructures and Ag<sub>x</sub>O films with controlled silver content. Suitable reduction process of Ag<sub>2</sub>O to Ag would be also benefit for removing of native oxide layer from silver structures (SERS substrates etc.) after long storage. However, reports about reciprocal conversion of Ag<sub>x</sub>O into Ag in dry ambient (gas, plasma) are concentrated on application of reducing agents like H<sub>2</sub> or annealing in inert ambient [8][9]. In the first case, the reducing agent can involve undesirable reactions with other materials of microdevice. In the second case, high temperature can limit choice of materials used in fabrication process. Nevertheless, publications about conversion of Ag<sub>x</sub>O into Ag without reducing agents are

occasional and devoted to interaction of Ag<sub>x</sub>O surface with energetic particles.

In this paper, we propose to use inert gas plasma for dry reduction of silver oxide films. It is demonstrated that conversion of Ag<sub>x</sub>O in Ag is possible in a standard reactor for dry etching using Ar, He or N<sub>2</sub> plasma. The reduction rate is proportional to ionization degree of plasma, i.e., concentration of electrons near processed sample. Ag content in the obtained films depends on plasma gas and can be controlled in broad range by process parameters, including reduction time, pressure and rf power.

The paper is organized in a following way. In the subsequent Section II, details of sample preparation and measurement procedures are presented. In Section III, results of the work are demonstrated by scanning electron microscope (SEM) images, electrical measurements as well as  $\psi$ ,  $\Delta$  spectra and reflection spectra of the fabricated samples. In Section IV, possible reduction mechanism of Ag<sub>2</sub>O in inert gas plasma is discussed. In Section V, the conclusion is drawn.

## II. EXPERIMENTAL DETAILS

A crystalline Si wafer (100 mm in diameter, 0.5-mm-thick, <100>) was used as a substrate. To increase accuracy of optical measurements, a 609 nm thick SiO<sub>2</sub> layer was prepared by thermal oxidation of the Si wafer. A 15 nm thick silver layer was deposited by electron-beam evaporation with the deposition rate of 0.3 nm/s and base pressure  $2 \times 10^{-7}$  Torr. All plasma treatments were made in two identical parallel plate reactors, which differ by sample position in a reactor. In the plasma etching (PE) reactor the sample was fixed on grounded electrode, in the reactive ion etching (RIE) reactor the sample was fixed on isolated electrode. Metal deposition and plasma treatments were done at room temperature.

Plasma oxidation was done in PE reactor during 90 seconds at oxygen flow of 100 sccm, pressure 1000 mTorr and rf power 20W. Several identical Ag<sub>x</sub>O samples were prepared to compare reduction in different conditions. For this purpose the whole wafer was cut on chips ( $2 \times 2$  cm<sup>2</sup>), which were further processed separately, but at the same pressure 500 mTorr and during the same time 60 s. The sample #1 was treated in RIE reactor at Ar flow 50 sccm, the samples #2, #3 were processed in PE reactor at flow 500 sccm of He and N<sub>2</sub>, respectively. Diluted ammonia solution (NH<sub>3</sub> 25 % from Honeywell) NH<sub>3</sub>:H<sub>2</sub>O = 1:1 was used for selective etching of Ag<sub>2</sub>O. This treatment does not affect on Ag, Si and SiO<sub>2</sub>. All samples were etched during 20 s.

Silver film was deposited in e-beam evaporation system IM-9912 (Instrumenti Mattila Oy, Finland). Plasma treatments were done in 13.56 MHz driven parallel electrode reactors Plasmalab 80 Plus (Oxford Instruments Plasma Technology). To investigate the prepared samples, plane-view image observations were performed in Zeiss Supra 40 field emission scanning electron microscope. Spectroscopic ellipsometry (SE) measurements in the range of 700–1700 nm at the angle 70° were done by spectroscopic ellipsometer SE 805 (SENTECH Instruments GmbH). Sheet resistance of films was measured by four points probe method. Reflectance measurements were carried out using a FilmTek 4000 (Scientific Computing International, USA) reflectometer at normal light incidence in the spectral range 400–1700 nm.

### III. RESULTS

In this section, the results of sequential oxidation of as deposited silver film and reduction of obtained silver oxide film are reported. To justify silver oxidation and Ag<sub>x</sub>O reduction, comparison of electrical, optical and chemical properties is performed.

#### A. Oxidation

In the beginning, reflection measurements for as deposited and plasma-oxidized silver films were made. Due to thick SiO<sub>2</sub> layer (609 nm), reflection from the Si substrate and low absorption in the upper layer, interference effects have been observed in both films (Fig. 1). It was noted that interference maxima of the silver film at 570 nm and 830 nm correspond to interference minima of the Ag<sub>x</sub>O film at the same wavelengths. Taking into account negligible optical thickness of the upper layer (less than  $\lambda/8$ ) and identical thicknesses of SiO<sub>2</sub> layers, this fact can be only explained by different phase shift upon reflection from Ag and Ag<sub>x</sub>O layers. Difference in phase shift is close to 180°. It means that the original metal layer has been converted into dielectric one after oxidation [10]. The formation of silver oxide is also evident from wet etching in ammonia solution. Silver film remains invariable, but Ag<sub>x</sub>O film is totally removed. The SEM images also confirm difference between as deposited and oxidized silver

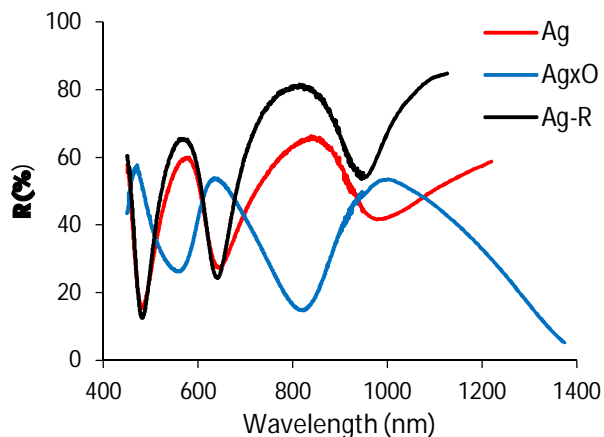


Figure 1. Reflection spectra of as deposited, oxidized and reduced (sample #2) Ag films.

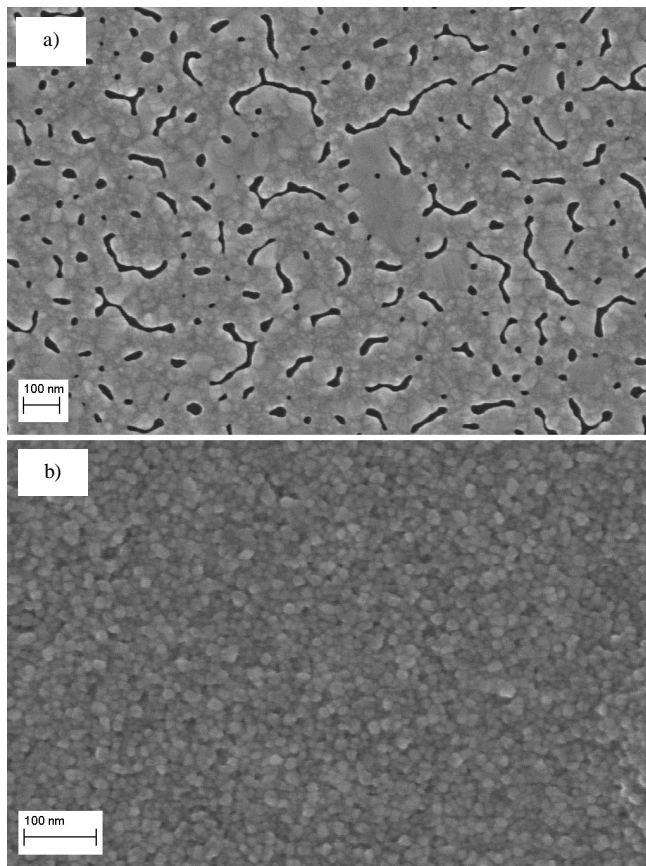


Figure 2. SEM images of as deposited (a) and oxidized (b) Ag films.

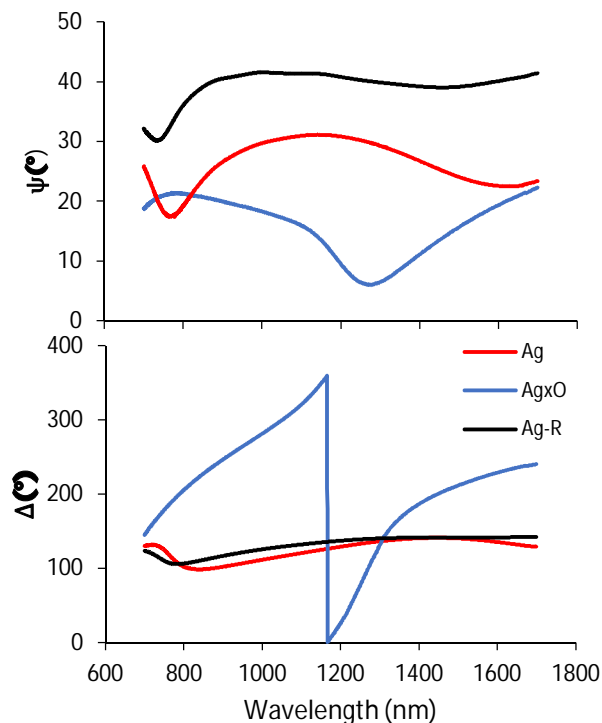


Figure 3.  $\psi$ ,  $\Delta$  spectra of as deposited, oxidized and reduced (sample #1) Ag films.

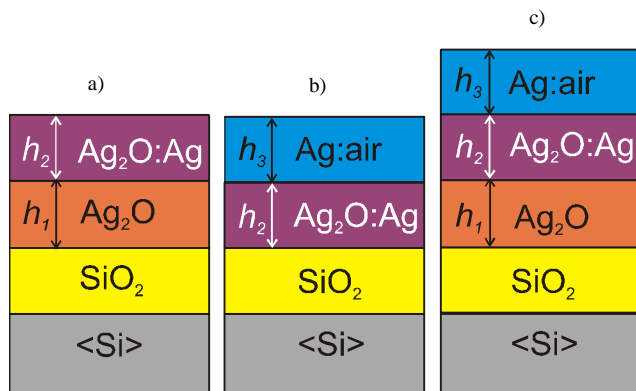


Figure 4. Optical models of  $\text{Ag}_x\text{O}$  (a), Ag reduced in He or Ar (b), Ag reduced in  $\text{N}_2$  (c).

films (Fig. 2). The discontinuous Ag film, including voids of random shape converts in agglomeration of closely packed crystallites. Cubic shape of crystallites resembles cubic crystalline structure of  $\text{Ag}_2\text{O}$ .

To measure optical constants of oxidized silver, SE was used. It is based on measurement of ellipsometric angles  $\psi$ ,  $\Delta$  in the range of wavelengths. After that the sample is described by simplified model from several optical layers and  $\psi$ ,  $\Delta$  are calculated for the model. Then, matching between measured and calculated  $\psi$ ,  $\Delta$  is done for different parameters of optical layers. The obtained  $\psi$ ,  $\Delta$  spectra of as deposited and oxidized silver films are given in Fig. 3. Totally different  $\psi$ ,  $\Delta$  curves before and after oxidation confirm conversion of Ag into  $\text{Ag}_x\text{O}$ .

To extract optical constants of the oxidized silver, the ellipsometric spectra were analyzed by model with layered structure. The model contains the pure  $\text{Ag}_2\text{O}$  layer (thickness  $h_1$ ) and the  $\text{Ag}_2\text{O}:\text{Ag}$  layer (thickness  $h_2$ ), as shown in Fig.4a. The  $\text{Ag}_2\text{O}:\text{Ag}$  composite was described in the assumption that it consists of  $\text{Ag}_2\text{O}$  matrix and Ag inclusions. The dielectric function of composite was calculated according to the Bruggemann effective-medium approximation (EMA). The unknown dielectric function of the  $\text{Ag}_2\text{O}$  was found by using Tauc-Lorentz dispersion formula with two oscillators. Parameters of these Lorentz oscillators are linked to imaginary part of the dielectric function and are listed in Table I.  $A_i$  is related to strength of the  $i$ -th absorption peak ( $i=1,2$ ),  $C_i$  is the damping coefficient of the  $i$ -th oscillator,  $E_i$  is the energy position of the  $i$ -th peak. Two additional parameters are optical band gap energy  $E_g = 0.21$  eV and high frequency dielectric constant  $\epsilon_\infty = 1.06$ .

TABLE I. PARAMETERS OF  $\text{Ag}_2\text{O}$  MODEL

Oscillator no.	A (eV)	E (eV)	C (eV)
1	7,30	4,27	0,15
2	20,80	3,20	2,40

The obtained model parameters for  $\text{Ag}_x\text{O}$  are given in Table II. Silver fraction in the composite layer  $\text{Ag}_2\text{O}:\text{Ag}$  is 0.07 and total thickness of the layer ( $h_1+h_2$ ) has increased to 34.5 nm after oxidation. The wavelength dependences of the extracted refractive index  $n$  and extinction coefficient  $k$  for  $\text{Ag}_2\text{O}$  are shown in Fig. 5. Both of them are higher than

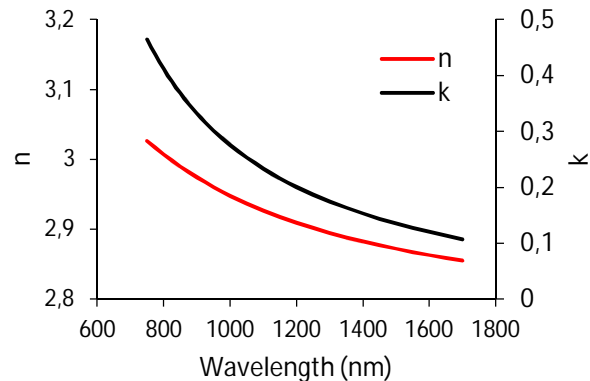


Figure 5. Optical constants of  $\text{Ag}_x\text{O}$ .

reported values for sputtered  $\text{Ag}_2\text{O}$  [4]. Both of them follow normal dispersion, i.e., decrease for longer wavelength in contrast to silver optical constants, which increase with wavelength. The purpose of optical calculations is justification of oxidation or reduction reactions in plasma ambient. In this context, absolute values of optical constants are not so significant as their variations in response on process parameter changing.

### B. Reduction

The wafer with silver oxide was cut in chips for reduction experiments in different conditions. In Fig. 1, reflection

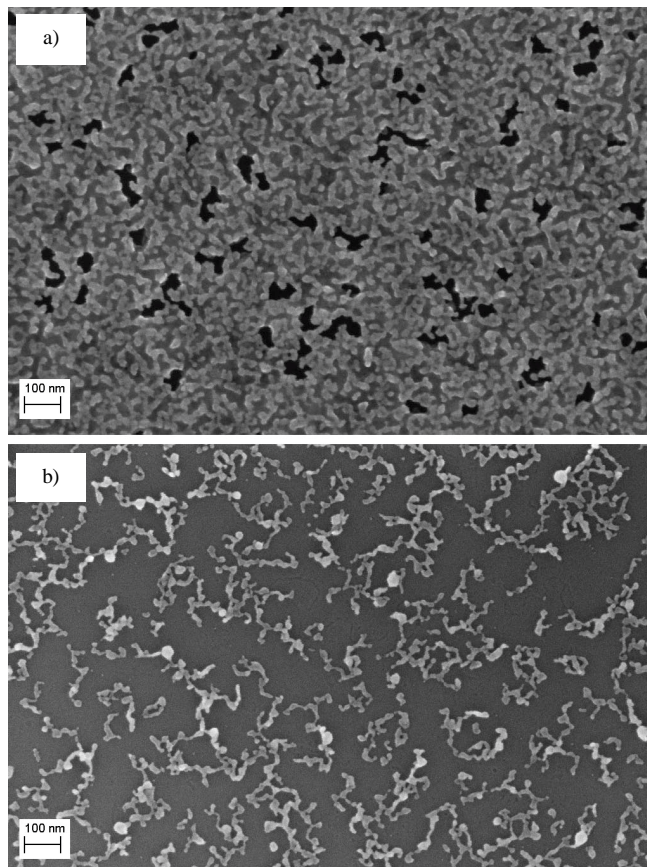


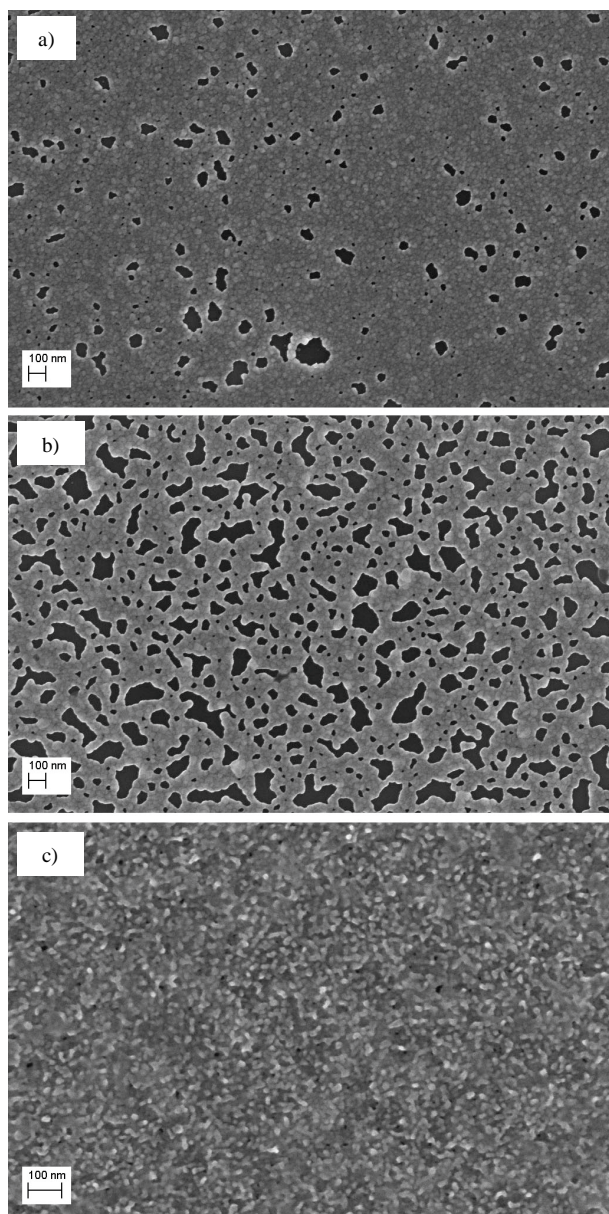
Figure 6. SEM images of the sample #3 after reduction (a) and after  $\text{NH}_3$  etching (b).

TABLE II. SAMPLE PREPARATION PARAMETERS AND MEASUREMENT RESULTS

Sample	Reactor	Gas	Power, W	$\rho$ , $\Omega$ m	Ag <sub>2</sub> O	Ag <sub>2</sub> O:Ag		Ag:air		Total	
					nm	nm	Ag <sup>a</sup>	nm	air <sup>b</sup>	Thickness, nm	Ag <sup>a</sup>
Ag				$7,1 \times 10^{-8}$						15,0	
Ag <sub>2</sub> O	PE	O <sub>2</sub>	35	$6,4 \times 10^{-1}$	18,0	16,5	0,07			34,5	0,03
#1	RIE	Ar	12	$8,0 \times 10^{-8}$		6,9	0,84	14,3	0,05	21,2	0,91
#2	PE	He	20	$9,7 \times 10^{-8}$		12,5	0,82	8,8	0,18	21,2	0,82
#3	PE	N <sub>2</sub>	20	$1,3 \times 10^{-6}$	6,0	6,9	0,30	10,2	0,44	23,1	0,34

a. Ag fraction in the layer.

b. Air fraction in the layer.


 Figure 7. SEM images of the samples reduced in Ar (a), He (b) and N<sub>2</sub> (c) plasma.

spectra of original (Ag) and reduced (Ag-R) silver (sample #2) are compared. The coinciding maxima and minima of Ag and Ag-R prove conversion of semiconductor Ag<sub>x</sub>O into metal Ag. Etching in ammonia solution does not affect on samples processed in Ar and He plasma (#1 and #2, respectively), but removes central part of sample #3, processed in N<sub>2</sub> plasma. Only 4 mm wide strip of changed colour was left around sample perimeter after ammonia processing. Fig. 6 shows SEM images of the sample #3 before and after wet etching in the edge area. The observed changing is possible, if the film consists of Ag<sub>2</sub>O and Ag. After wet etching Ag<sub>2</sub>O is removed, leaving Ag phase on the substrate. SEM images of the central areas of the Ag<sub>x</sub>O film processed in Ar (sample #1), He (sample #2) and N<sub>2</sub> (sample #3) plasma are shown in Fig. 7. While Ar and He processed samples demonstrate similar images of silver films with different fragmentation, the image of the sample #3 is more complicate. It can be considered as dark background from Ag<sub>x</sub>O at which bright silver inclusions are visible.

The  $\psi$ ,  $\Delta$  spectra of reduced Ag<sub>x</sub>O for the sample #1 are shown in Fig. 3. They look very similar to spectra of as deposited silver. Reconstruction of sample layers after reduction was done by using optical models shown in Fig. 4b and Fig. 4c. The composite Ag<sub>2</sub>O:Ag layer was described by EMA and the model for Ag<sub>2</sub>O obtained at oxidation step (Table 1) was used. After that, only thickness and Ag content in layers were changed during matching. In such a way, efficiency of reduction can be estimated by total Ag content in films.

The results of optical measurements are given in Table II. The samples processed in Ar and He can be considered consisting of Ag<sub>2</sub>O:Ag layer (thickness  $h_2$ ) and rough silver layer (thickness  $h_3$ ), modeled as Ag:air composite. The sample processed in N<sub>2</sub>, additionally includes pure Ag<sub>2</sub>O layer (thickness  $h_1$ ) at SiO<sub>2</sub> interface. The total Ag fraction in samples was calculated as average of layer Ag contents according to thickness weight function (fraction of layer thickness in total thickness). Total thickness of all reduced samples is practically the same (Table II) and much less than thickness of Ag<sub>x</sub>O film. The thicknesses of as deposited and reduced silver cannot be compared, because they were estimated by quartz microbalance and SE, respectively.

Effect of process parameters on reduction result was studied by monitoring resistivity and Ag content. Fig. 8 demonstrates dependence of these characteristics on process

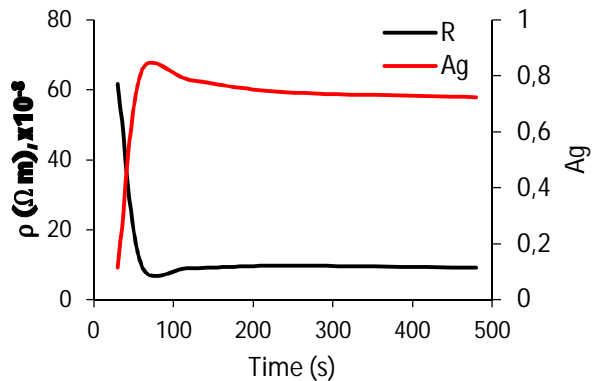


Figure 8. Dependence of resistivity and Ag content on reduction time for film reduced in He plasma.

time for PE reactor with He plasma. Fig. 9 and Fig. 10 show variation of resistivity and Ag content with process pressure and rf power, respectively, in RIE reactor with Ar plasma. The fullest reduction happens when processes is done during 60 s at pressure 125 mTor. Mirror like behavior of curves for resistivity and Ag content reflect the fact that Ag inclusions are responsible for electrical conductivity of the samples.

#### IV. DISCUSSION

The obtained film parameters and SEM images demonstrate synthesis and decomposition of silver oxide during forward reaction of oxidation and reverse reaction of reduction, respectively. Indeed, total transformation of optical and electrical properties of the film after O<sub>2</sub> plasma processing and full restoration of these properties after inert gas plasma treatment (Table II), can be reasonably explained by formation of silver oxide Ag<sub>x</sub>O and its conversion into silver, respectively. In this section, we discuss the possible reduction mechanism of silver oxide.

Any sample treated in plasma is bombarded by electrons and ions. The maximum energy of bombarding ions depends on the sample potential. In the PE reactor, the processed sample has potential around 10V relatively plasma. In the RIE reactor, the sample potential is equal to dc self-bias (16 V for sample #1) and depends on process parameters. The beginning of sputtering is defined by threshold energy, which is equal 25 eV and 34 eV for silver sputtering by Ar and He ions,

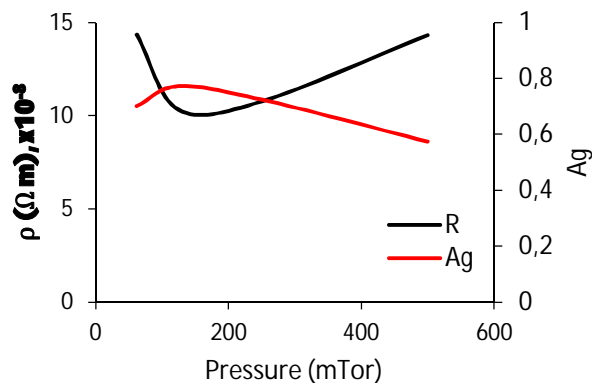


Figure 9. Dependence of resistivity and Ag content on process pressure for film reduced in He plasma.

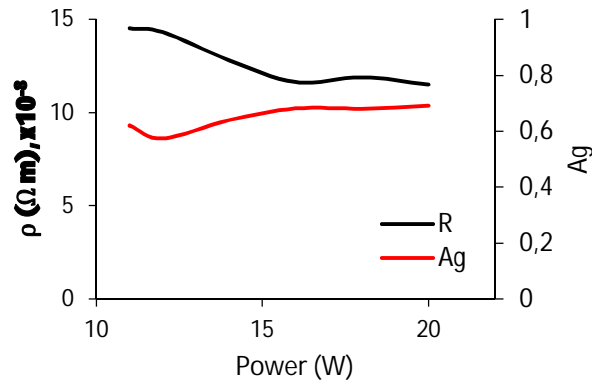


Figure 10. Dependence of resistivity and Ag content on rf power for film reduced in He plasma.

respectively [11][12]. Therefore, ion energy for He reduction process in the PE reactor is less than threshold sputtering level and sputtering effect cannot be responsible for Ag<sub>x</sub>O reduction.

Energy required to break chemical bonds can be delivered in different ways. For example, silver oxide is decomposed on silver and atomic oxygen during low temperature treatment (200 °C) or under UV irradiation. It means that Ag<sub>2</sub>O has low bond energy and Ag-O bond can be easily broken. Electron bombardment is often used for breaking chemical bonds. Low energy primary electrons (160 eV) are able to generate secondary electrons, displace oxygen anions and reduce oxides, e.g., TiO<sub>2</sub> [13]. In case of Ag<sub>2</sub>O, secondary electron emission is strong enough and starts when primary electron energy exceeds 5 eV. Therefore, reduction of Ag<sub>2</sub>O by low energy electrons is also possible and mechanism of plasma reduction is decomposition of Ag<sub>2</sub>O on Ag and atomic oxygen under bombardment of electrons ejected from plasma. It means, that reduction rate depends on electron concentration in plasma or degree of its ionization.

At low rf power and low electron energy, most particle collisions in plasma lead to molecule dissociation and excitation, but not to ionization [14]. In monoatomic gases (Ar, He), dissociation is not possible and ionization is more effective than in diatomic gases (N<sub>2</sub>). In other words, plasma concentration is higher for Ar and He, than for N<sub>2</sub>. In case of sample #3 (N<sub>2</sub> plasma), it explains the lowest reduction rate, demonstrated by the highest resistivity, the lowest Ag fraction and totally different morphology of reduced film in comparison with He and Ar processed samples. Deviation in plasma concentration leads also to different reduction efficiency in Ar and He plasmas. Ionization energy for He and Ar atoms is 25 eV and 16 eV, respectively. Lower ionization energy leads to higher electron concentration in Ar plasma.

Increasing of Ag content with rf power (Fig. 10) is in accordance with dependence of reduction rate on plasma concentration, which is proportional to electrical field strength. However, at rf power higher than 16W, trends in behavior of  $\rho$  and Ag content (Fig. 10) are changed. At high power, bias exceeds 25 V, ion energy is above threshold sputtering energy of Ag and sputtering effect becomes significant. It results in preferable silver sputtering from Ag<sub>2</sub>O:Ag composite.

Plasma reduction of silver oxide requires only electron impact and can take place in any plasma, e.g., in oxygen one. Silver film oxidized by oxygen plasma is simultaneously exposed to electron irradiation. Electrons facilitate  $\text{Ag}_2\text{O}$  reduction at the same time, when atomic oxygen oxidizes silver. As a result full Ag oxidation does not happen and silver inclusions are observed in  $\text{Ag}_2\text{O}$  obtained in both PE and RIE reactors (Table II).

## V. CONCLUSION

Standard parallel plate reactor can be used both for plasma oxidation of silver, and for plasma reduction of silver oxide. In contrast to oxidation, which happens in atomic oxygen ambient, reduction does not require chemically active species and is done in inert gas plasma. Possible reduction mechanism is connected with breaking of Ag-O bonds and generation of secondary electrons. Bond breaking happens due to interaction of silver oxide with electrons and ions of plasma. Rate of plasma reduction is proportional to plasma concentration and can be tuned by plasma gas, rf power and working pressure. Morphology of silver films obtained by processing of  $\text{Ag}_x\text{O}$  in plasma depends on reduction rate and differs for He, Ar and  $\text{N}_2$  plasmas.

Sequential silver oxidation and reduction in one reactor may be useful in obtaining of  $\text{Ag}_x\text{O}$  films with controlled silver content.

## ACKNOWLEDGMENT

This research was undertaken at the Micronova Nanofabrication Centre, supported by Aalto University.

## REFERENCES

- [1] E. C. Le Ru and P. G. Etchegoin, *Principles of Surface-Enhanced Raman Spectroscopy and Related Plasmonic Effects*, Amsterdam: Elsevier, pp. 181-183, 2008.
- [2] J. Tominaga, "The application of silver oxide thin films to plasmon photonic devices," *Journal of Physics: Condensed Matter*, vol. 15, pp. R1101-R1122, Jun 2003.
- [3] G. Saroja, V. Vasu and N. Nagarani, "Optical Studies of  $\text{Ag}_2\text{O}$  Thin Film Prepared by Electron Beam Evaporation Method," *OJMetal*, vol. 3, pp. 57-63, 2013.
- [4] Gao X.-Y. et al., "Analysis of the dielectric constants of the  $\text{Ag}_2\text{O}$  film by spectroscopic ellipsometry and single-oscillator model," *Physica B*, vol. 405, pp. 1922-1926, 2010.
- [5] A. C. Nwanya, P. E. Ugwuoke, B. A. Ezekoye, R. U. Osuji, and F. I. Ezema, "Structural and Optical Properties of Chemical Bath Deposited Silver Oxide Thin Films: Role of Deposition Time," *Advances in Materials Science and Engineering*, vol. 2013, pp. 1-8, Mar 2013.
- [6] W. M. Moor and P. J. Codella, "Oxidation of Silver Films by Atomic Oxygen," *J. Phys. Chem.*, vol. 92, pp. 4421-4426, Jul 1988.
- [7] M. L. Zheludkevich et al., "Oxidation of Silver by Atomic Oxygen," *Oxidation of Metals*, vol. 61, pp. 39-48, Feb 2004.
- [8] G. Schimo, A. M. Kreuzer, and A. W. Hassel, "Morphology and size effects on the reduction of silver oxide by hydrogen," *physica status solidi (a)*, vol. 212, pp. 1202-1209, June 2015.
- [9] C. C. Tseng, J. H. Hsieh, C. H. Lin, and W. Wu, "Effects of deposition and annealing temperatures on the electrical and optical properties of  $\text{Ag}_2\text{O}$  and  $\text{Cu}_2\text{O}$ - $\text{Ag}_2\text{O}$  thin films," *J. Vac. Sci. Technol. A*, vol. 28, pp. 791-794, 2010.
- [10] Philip W. Baumeister, *Optical coating technology*, Bellingham: SPIE Press, pp. 2-23 - 2-34, 2004.
- [11] A. J. van Roosmalen, J. A. G. Baggerman, and S. J. H. Brader, *Dry Etching for VLSI*, New York: Plenum Press, pp. 65-66, 1991.
- [12] E. Hotston, "Threshold energies for sputtering," *Nucl. Fusion*, vol. 15, pp. 544-547, 1975.
- [13] R. Patel et al., "The defective nature of the  $\text{TiO}_2(110) (1 \times 2)$  surface," *J. Vac. Sci. Technol. A*, vol. 15, pp. 2553-2556, Sep/Oct 1997, doi: 10.1116/1.580769.
- [14] M. Lassus and J-P. Founaud, "Modern physics brings semiconductor technology to a turning point," *Microelectronics Reliability*, vol. 16 (4), pp. 367-387, 1977.

# Quantum Hexagonal Quadrature Amplitude Modulation

YoungJun Kim

School of Electrical Engineering  
Korea University  
Seoul, South Korea  
Email: mkeeper@korea.ac.kr

Young-Chai Ko

School of Electrical Engineering  
Korea University  
Seoul, South Korea  
Email: koyc@korea.ac.kr

**Abstract**—In this paper, we propose the hexagonal quadrature amplitude modulation (QAM)-type modulation for continuous-variable quantum communication systems. Our proposed hexagonal QAM modulation provides less detection error, which occurs in discriminating non-orthogonal quantum states, compared to the previous modulation schemes such as phase shift keying (PSK)-type modulation or rectangular QAM-type modulation. Square root measurement (SRM) is used in the receiver to decrease the detection error probability and receiver complexity. The theoretical detection error rate for the hexagonal QAM modulation is obtained by form of square root of matrix. The detection error rate is verified by Monte Carlo simulation.

**Keywords**—Quantum communication, hexagonal QAM, continuous variables, coherent states

## I. INTRODUCTION

As the usage of personal communication devices increases, the communication security system becomes more important than ever. The quantum cryptography using quantum key distribution (QKD) is regarded as the future possible technology to guarantee unconditional security [1]. Basically, the quantum cryptography is based on the fact that nonorthogonal quantum states can not be distinguished with certainty [2]. Note that the detection of coherent states is accomplished by quantum measurement which naturally brings about the detection errors.

In this paper, we consider a quantum detection problem. Alice transmits classical information key to Bob through quantum channel. Both Alice and Bob prepare a set of quantum coherent states, and Alice chooses one of the states corresponding to the message. The receiver, Bob, extracts the message from a quantum measurement of the received quantum state. Because the set of coherent states Alice and Bob use are not orthogonal to be general, all measurement can bring about the detection error. Our design goal is to build the shared set of quantum states and to build the quantum measurement.

This quantum detection problem has been researched in many previous papers [3]–[6]. In [6], Yuen contrived a new quantum cryptography which also ensures the unconditional security. The protocol invented by Yuen is called Y-00 protocol named after himself. In Y-00, a set of phase shift keying (PSK) type states is considered. Security is from the detection error rate gap between Bob and Eve, an eavesdropper, where Bob shares an initial secret key string with Alice but Eve does not. Y-00 protocol opened a new type of QKD, *continuous variable quantum key distribution (CV-QKD)*, by using coherent states as information carrier.

Positive operator valued measurement (POVM) is a set of Hermitian positive semidefinite operators. In quantum mechan-

ics, all observable quantity is obtained by a special quantum transaction called *quantum measurement*. By subjecting the state to a quantum measurement, we can obtain a value corresponding to the quantum state. POVM is widely used to measure quantum states because it is easy to realize in a physical system and because it has good mathematical properties for performance analysis [2] [7].

The QAM provides better performance than the PSK in terms of the error probability in higher spectral efficiency case [8]. For this reason, QAM is adopted in many recent communication standards to meet the demand of high speed data rate. The constellation of QAM has several shapes such as square QAM, circular QAM, hexagonal QAM and so on. It is notable that the hexagonal QAM provides the largest minimum Euclidian distance (ED) given the energy constraint compared to other QAM schemes. Hexagonal QAM gives less error rate performance than rectangular QAM but hexagonal QAM is not popular in practical communication systems because of its high implementation complexity compared to other QAM shapes [9].

For PSK scheme, which has the circular symmetric quantum states set, the square root measurement (SRM) detection has been proven to provide the minimum detection error probability [2]. On the other hand, for QAM state, which does not have the circular symmetric quantum states set, the optimum detection scheme in terms of error probability has not been known yet. However, SRM detection can provide quite a good performance when the average number of photons of coherent states,  $N_s$ , is sufficiently large based on which the application of SRM detection to QAM has been studied in the literature [10]. The set of QAM state is not circular symmetric but Kato employed SRM for QAM state detection problem. Optimality of SRM for QAM state detection is not proven. But detection probability of QAM state using SRM gives less detection error than PSK state using SRM with same energy constraint.

In SRM detection, the ED between two states is the dominant factor for error detection. In a state set, we have shown in a previous study [11] that the average detection error probability is dominant with the minimum ED among the states of the set. We have shown that circular QAM scheme can reduce the detection error rate by enlarging the minimum ED under a given energy constraint. Moreover, hexagonal QAM scheme has larger minimum ED than circular QAM scheme so we can expect that hexagonal QAM scheme gives less detection error rate than PSK, rectangular QAM and circular QAM.

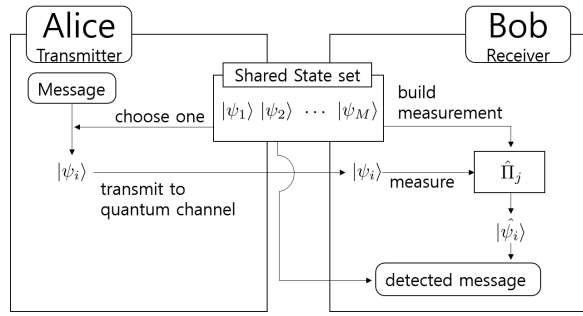


Figure 1. System description

This paper is organized as follows. In Section 2, the mathematical representation of our considering system is described. In Section 3, the SRM detection scheme in the receiver is mathematically described. In Section 4, our new hexagonal QAM scheme is suggested. In Section 5, we show the detection error performance of our hexagonal QAM scheme with SRM detection in a numerical way. Finally, Section 6 concludes the paper.

## II. MATHEMATICAL SYSTEM REPRESENTATION

Let us consider the detection problem of quantum states illustrated in Figure. 1. Alice chooses one of pure states in a set of coherent states and sends it to Bob. Then Bob measures the received state and chooses one of the states based on the minimum detection error criterion. Note that an error occurs if the state chosen by Bob is different from Alice's state.

We consider a pure state set  $\rho$  of size  $M$  in Hilbert space  $\mathcal{H}_s$ . Each state of  $\rho$  is represented by density operator  $\rho_i$  which is non-negative and unit trace.

$$\rho_i \geq 0, \quad \text{Tr}[\rho_i] = 1 \quad (i = 1, 2, \dots, M). \quad (1)$$

From the pure state assumption, each state can be also represented in vector form such as

$$\rho_i = |\psi_i\rangle \langle \psi_i| \quad (2)$$

where  $|\psi_i\rangle$ , called *ket*  $\psi_i$ , is Dirac's bra-ket notation of the quantum state and  $\langle \psi_i|$ , called *bra*  $\psi_i$ , is the dual state of  $|\psi_i\rangle$ .

A coherent state  $|\alpha\rangle$  is an eigen state of photon annihilation operator,  $a$  [12],

$$a|\alpha\rangle = \alpha|\alpha\rangle \quad (3)$$

and can be expressed using the representation in the basis of number states,  $|n\rangle$ ,

$$|\alpha\rangle = e^{-\frac{|\alpha|^2}{2}} \sum_{n=0}^{\infty} \frac{\alpha^n}{\sqrt{n!}} |n\rangle. \quad (4)$$

Note that  $\alpha$  can be an arbitrary complex value where the real part of  $\alpha$  relies on the position of the photon and the imaginary part of  $\alpha$  relies on the momentum of the photon [13].

For detection of the received states, we employ the POVM  $\hat{\Pi}_j$  which satisfies the following relations

$$\hat{\Pi}_j \geq 0, \quad (5)$$

and

$$\sum_{j=1}^M \hat{\Pi}_j = \hat{I}. \quad (6)$$

Let us denote  $P(j|i) \triangleq P(\rho_j|\rho_i)$  as the conditional probability that the quantum state  $\rho_i$  is decided as  $\rho_j$ . Then  $P(j|i)$  can be represented as

$$P(j|i) = \text{Tr}[\hat{\Pi}_j \rho_i]. \quad (7)$$

Note that the value  $P(j|i)$  for  $(j \neq i)$  represents the decision error probability. Then the average probability of decision error  $P_e$  is given by

$$\begin{aligned} P_e &= \sum_{i=1}^M q_i \sum_{j=1(\neq i)}^M P(j|i) \\ &= 1 - \sum_{i=1}^M q_i P_i(i|i) \end{aligned} \quad (8)$$

where  $q_i$  is a *a priori* probability of the quantum state  $\rho_i$  satisfying

$$\sum_{i=1}^M q_i = 1, \quad q_i \geq 0. \quad (9)$$

To simplify the discussion, we focus on the equal probable case, that is  $q_i = \frac{1}{M}$  for all  $i$ .

## III. DETECTION ERROR PERFORMANCE OF SQUARE ROOT MEASUREMENT

Quantum measurement is defined as a set of operators. In quantum mechanics, an operator is similar to a system in classical mechanics. As long as the state in quantum is represented in a vector form, the quantum operator can also be represented in a matrix form. POVM is a good example of quantum measurement.

Now, we consider SRM for detection. SRM is known as the optimal detection measurement scheme in distinguishing circular symmetric states, i.e., PSK states, in terms of detection error rate. Note that when the state set is not circular symmetric, the optimal detection measurement scheme is not known yet. However, as shown in [14]–[17], SRM is often employed for non-symmetric case since it can be built by manipulating the shared state set. Here, we also employ SRM for the signal detection of hexagonal states considered in. The hexagonal states set considered in this paper is not circular symmetric. But SRM has been employed in many systems because of its good properties [18].

The detection operator of SRM, denoted as  $\hat{\Pi}_j$  for the  $j$ -th state is defined as [17]:

$$\begin{aligned} \hat{\Pi}_j &= |\mu_j\rangle \langle \mu_j| \\ |\mu_j\rangle &= \hat{G}^{-1/2} |\psi_j\rangle \\ \hat{G} &= \sum_{i=1}^M |\psi_i\rangle \langle \psi_i|. \end{aligned} \quad (10)$$

We can easily prove that SRM,  $\hat{\Pi}_j$ , satisfies (5) and (6) just by substituting  $\hat{\Pi}_j$  into (5) and (6). It means that SRM is a class of POVM and we can get the advantage of POVM mentioned in Section I.

In the case of using SRM in detection, the conditional detection error probability  $P(j|i)$  can be calculated by square root of the Gram matrix  $G$

$$p(j|i) = \left| (G^{1/2})_{ji} \right|^2 \quad (11)$$

where the Gram matrix  $G$  is the Hermitian matrix whose entries are inner products of coherent states [2]

$$G = \begin{bmatrix} \langle \psi_1 | \psi_1 \rangle & \cdots & \langle \psi_1 | \psi_M \rangle \\ \vdots & \ddots & \vdots \\ \langle \psi_M | \psi_1 \rangle & \cdots & \langle \psi_M | \psi_M \rangle \end{bmatrix}. \quad (12)$$

From (4), the inner product of two coherent states can be calculated as

$$\begin{aligned} \langle \alpha | \beta \rangle &= e^{-\frac{|\alpha|^2 + |\beta|^2}{2}} \sum_{m=0}^{\infty} \sum_{n=0}^{\infty} \frac{\alpha^{*m} \beta^n}{\sqrt{m!n!}} \langle m | n \rangle \\ &= e^{-\frac{|\alpha|^2 + |\beta|^2}{2}} \sum_{n=0}^{\infty} \frac{(\alpha^* \beta)^n}{n!} \\ &= e^{-\frac{|\alpha|^2 + |\beta|^2}{2} + \alpha^* \beta} \\ &= A_{\alpha\beta} \exp j\theta_{\alpha\beta} \end{aligned} \quad (13)$$

where

$$A_{\alpha\beta} = \exp \left[ -\frac{1}{2} ((\alpha_R - \beta_R)^2 + (\alpha_I - \beta_I)^2) \right] \quad (14)$$

$$\theta_{\alpha\beta} = [\alpha_R \beta_I - \alpha_I \beta_R]. \quad (15)$$

and

$$\alpha_R = \Re\{\alpha\}, \alpha_I = \Im\{\alpha\}, \beta_R = \Re\{\beta\}, \beta_I = \Im\{\beta\}.$$

In (11), we point out that the off-diagonal element of square root of the Gram matrix directly influences the conditional detection error probability. In (12), we can see that the off-diagonal elements of the Gram matrix is in inner product form between two different states. In (14), the Euclidian distance between two different states is the dominant factor in the amplitude of inner product between the states. Now, we can say that a states set with large minimum ED can reduce the detection error rate. Hence, it is desired to make the signals spread as far as they can in given signal average energy constraint.

#### IV. MINIMUM EUCLIDIAN DISTANCE MAXIMIZING MODULATION : HEXAGONAL QAM

In classical communication systems, the hexagonal QAM scheme is used because of low peak to average power ratio [9] or used in the case considering multiple retransmission system for the automatic repeat request [19]. But hexagonal QAM scheme is rarely used because it can not be demodulated by the two dimensional projective way which deduces the complexity of the receiver.

To detect quantum coherent states, the two dimensional projective way is limited by Heisenberg type uncertainty. In this paper, we consider SRM detection and the detection error performance of SRM is affected by the minimum ED among the states. The hexagonal QAM state gives the largest minimum ED under a given energy constraint.

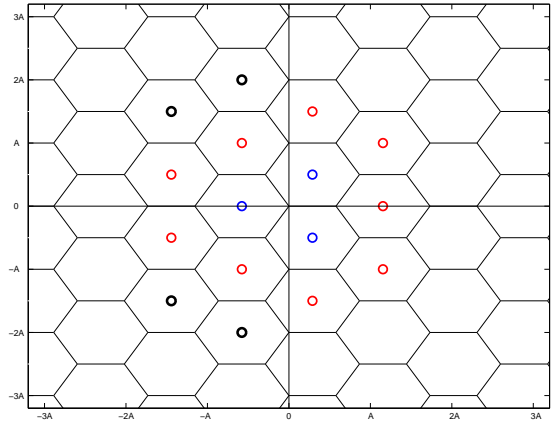


Figure 2. States set for 16-ary hexagonal QAM

The shape of constellation points of Hexagonal QAM is in the form of a shell. We can easily find the number of signals that make the complete shell, and that number is

$$3n^2, n \in \mathbb{N} \quad (16)$$

where  $n$  is the number of shells. Figure. 2 shows an example of quantum hexagonal QAM states for  $M = 16$  case. States for 16-QAM are denoted as

$$\begin{aligned} |\psi_1\rangle &= |A(-\frac{\sqrt{3}}{3})\rangle \\ |\psi_2\rangle &= |A(\frac{\sqrt{3}}{6} + j\frac{1}{2})\rangle \\ |\psi_3\rangle &= |A(\frac{\sqrt{3}}{6} - j\frac{1}{2})\rangle \\ &\vdots \\ |\psi_{16}\rangle &= |A(-\frac{\sqrt{3}}{3} + j2)\rangle \end{aligned} \quad (17)$$

where  $A$  is a real valued fundamental amplitude. Euclidian distance between most neighboring states is set to be  $A$ .

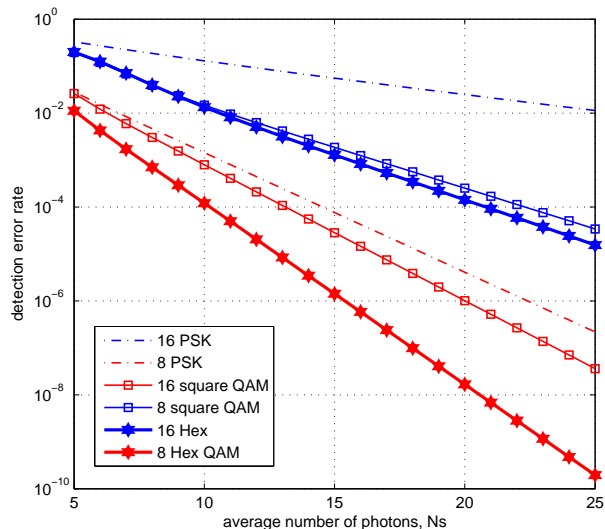
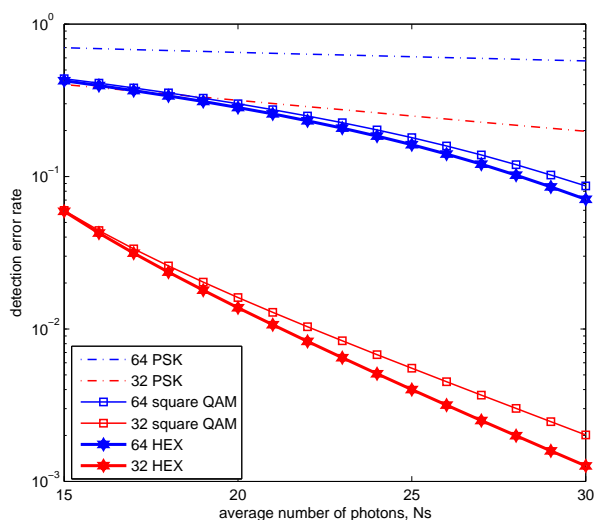
We can see that the first and the second shell is full of states, and the third shell has empty spaces. These empty spaces degrade data rate performance. In our quantum modulation, we consider uncoded classical information so the gap between  $2^n$  for classical bit and (16) for hexagonal QAM symbol degrades the rate.

#### V. NUMERICAL RESULT

For comparing the error rate of detection, the average value of the photon number,  $N_s$  is a common parameter which is defined as:

$$N_s = \sum_{i=1}^M q_i \langle \psi_i | \hat{n} | \psi_i \rangle \quad (18)$$

where  $\hat{n} = \hat{a}^\dagger \hat{a}$  is the number operator of the coherent state. The detection error probability is calculated by substituting (17) to (13), (12), (11) and (8). In (11), square root of Hermitian matrix is calculated by eigen value decomposition in MATLAB.


 Figure 3. Detection error rate for  $M = 8$  and  $M = 16$ 

 Figure 4. Detection error rate for  $M = 32$  and  $M = 64$ 

As seen in Figure 3, we can certify that all types of QAM schemes give less detection error rate than the PSK scheme. The rectangular QAM states are from [17]. The detection error rate of our hexagonal QAM scheme is less than other modulation schemes. And we can also see that the performance gain of our hexagonal QAM scheme is steady compared to the rectangular QAM case which works well in  $M = 16$  case but does not work well in  $M = 8$  case relatively. Figure 4 shows the detection error rates for higher order cases in large  $N_s$ . Our hexagonal QAM scheme also performs better than other schemes in detection error rate in higher order cases. Especially, we can find a cross-over between PSK scheme for  $M = 32$  and hexagonal QAM scheme for  $M = 64$ . It means that our hexagonal QAM state can carry more information bits and can give less detection error performance in some cases.

As the modulation size  $M$  grows, we need more photons to meet a certain detection error rate. Our hexagonal QAM scheme still has performance gain in higher modulation cases. The average number of photons to meet a certain detection error rate is still less in our hexagonal QAM state for higher order cases.

## VI. CONCLUSION

In this paper, we proposed a new hexagonal QAM scheme that reduces the detection error probability by maximizing the minimum ED between states in the constellation. We used SRM to detect the sent state. Numerical simulation showed that our hexagonal QAM gives less detection error rate under an average photon number constraint in several sizes of modulation.

## ACKNOWLEDGMENT

This research was supported by the MSIP (Ministry of Science, ICT and Future Planning), Korea, under the ITRC (Information Technology Research Center) support program (IITP-2016-R0992-16-1017) supervised by the IITP (Institute for Information & communications Technology Promotion)

## REFERENCES

- [1] D. Mayers, "Unconditional security in quantum cryptography," *J. of the ACM*, vol. 48, no. 3, pp. 351–406, 2001.
- [2] M. Ban, K. Kurokawa, R. Momose, and O. Hirota, "Optimum measurements for discrimination among symmetric quantum states and parameter estimation," *Int. J. of Theoretical Phys.*, vol. 36, no. 6, pp. 1269–1288, 1997.
- [3] C. W. Helstrom, "Bayes-cost reduction algorithm in quantum hypothesis testing (corresp.)," *IEEE Trans. Inform. Theory*, vol. 28, no. 2, pp. 359–366, 1982.
- [4] K. Kato and O. Hirota, "Quantum quadrature amplitude modulation system and its applicability to coherent-state quantum cryptography," in *Optics & Photonics 2005*. Int. Soc. for Optics and Photonics, 2005, pp. 589 303–589 303.
- [5] —, "Square-root measurement for quantum symmetric mixed state signals," *IEEE Trans. Inform. Theory*, vol. 49, no. 12, pp. 3312–3317, 2003.
- [6] H. P. Yuen, "KCQ: A new approach to quantum cryptography i. general principles and key generation," *arXiv preprint quant-ph/0311061*, 2003.
- [7] M. Ziman and V. Bužek, "Realization of positive-operator-valued measures using measurement-assisted programmable quantum processors," *Phys. Rev. A*, vol. 72, no. 2, p. 022343, 2005.
- [8] J. G. Proakis, *Digital Communications*. McGraw-Hill, 1995.
- [9] S. H. Han, J. Cioffi, and J. H. Lee, "On the use of hexagonal constellation for peak-to-average power ratio reduction of an ODFM signal," *IEEE Trans. Wireless Commun.*, vol. 7, no. 3, pp. 781–786, March 2008.
- [10] P. Hausladen and W. K. Wootters, "A pretty good measurement for distinguishing quantum states," *J. of Modern Optics*, vol. 41, no. 12, pp. 2385–2390, 1994.
- [11] Y. Kim and Y.-C. Ko, "Detection of quantum circular QAM signals," in *Int. Conv. Inform. and Commun. Technology*, Oct 2013, pp. 1078–1082.
- [12] H. P. Yuen, "Two-photon coherent states of the radiation field," *Phys. Rev. A*, vol. 13, no. 6, p. 2226, 1976.
- [13] P. Carruthers and M. M. Nieto, "Phase and angle variables in quantum mechanics," *Rev. Mod. Phys.*, vol. 40, pp. 411–440, Apr 1968. [Online]. Available: <http://link.aps.org/doi/10.1103/RevModPhys.40.411>
- [14] A. Peres and W. K. Wootters, "Optimal detection of quantum information," *Phys. Rev. Lett.*, vol. 66, no. 9, p. 1119, 1991.
- [15] M. Sasaki, K. Kato, M. Izutsu, and O. Hirota, "Quantum channels showing superadditivity in classical capacity," *Phys. Rev. A*, vol. 58, no. 1, p. 146, 1998.

- [16] M. Sasaki, T. Sasaki-Usuda, M. Izutsu, and O. Hirota, "Realization of a collective decoding of code-word states," *Phys. Rev. A*, vol. 58, no. 1, p. 159, 1998.
- [17] K. Kato, M. Osaki, M. Sasaki, and O. Hirota, "Quantum detection and mutual information for QAM and PSK signals," *IEEE Trans. Commun.*, vol. 47, no. 2, pp. 248–254, 1999.
- [18] Y. C. Eldar and G. D. Forney Jr, "On quantum detection and the square-root measurement," *IEEE Trans. Inf. Theory*, vol. 47, no. 3, pp. 858–872, 2001.
- [19] L. Snzeczinski and M. Bacic, "Constellations design for multiple transmissions maximizing the minimum squared euclidean distance," in *IEEE conf. Wireless Commun. and Networking*, vol. 2, March 2005, pp. 1066–1071 Vol. 2.

# The Formation of Black Glass with Ladder-like Silsesquioxanes

Sitarz Maciej

Faculty of Materials Science and Ceramics, AGH University of Science and Technology  
Cracow, Poland  
e-mail: msitarz@agh.edu.pl

**Abstract** - The main objective of this paper is to determine the process of formation of black glasses from ladder-like silsesquioxane precursors. Well-defined polysilsesquioxanes with ladder-like structure obtained via the sol-gel process allowed to control the amount of introduced carbon which allows us to control the properties of received glasses. Raman and middle infrared (MIR) spectroscopy research allowed to determine the structure of obtained materials and thus, to describe the process of formation of black glasses.

**Keywords**- silsesquioxanes; black glasses; SiOC.

## I. INTRODUCTION

Black glasses (SiOC glasses) are materials of amorphous silica structure, in which two  $O^{2-}$  ions are substituted by one  $C^{4-}$  anion (Figure 1). That type of substitution leads to a local increase in the density of bonds and therefore to a significant strengthening of the network. The ideal structure of black glasses contains only Si-O and Si-C bonds.

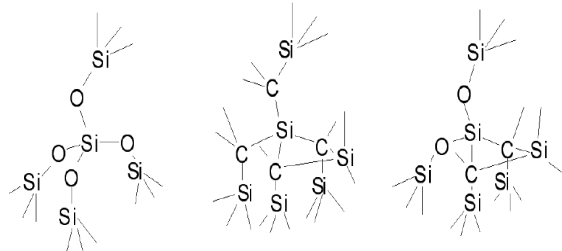


Figure 1. The structural formula of: silica  $SiO_2$  (left), SiC (center), silicon oxycarbide (right) [1].

Unfortunately, the silica glass structure can accept only a limited amount of carbon ions. Therefore, black glasses usually also contain so called free carbon (phase separation) - that is responsible for their black color.

The presence of free carbon and its structure has a tremendous impact on the thermal stability and mechanical properties of the glasses. Analysis of the literature shows that functional parameters of black glasses may vary within very wide limits, depending on the amount of free carbon and isomorphous substitution in the glass structure [2]-[9].

## II. EXPERIMENTAL

As it was mentioned, the main reason for the use of ladder-like polysilsesquioxanes as precursors of black glass was the need to ensure the stoichiometry of the glass. This allows to control the amount of Si-C bonds. The

$CH_3Si(OCH_3)_3$  (T units) and  $((CH_2Si(OC_2H_5)_2)$  (D units) were used as a silsesquioxane precursors. A mixture of T/D=2/1 was hydrolyzed using water and HCl catalyst to obtain ladder-like structures (P0). To obtain glassy  $SiC_xO_y$ , dried samples were subsequently heat-treated in a tube furnace at 200, 400, 600 and 800 °C temperature ranges.

## III. RESULTS AND DISCUSSION

The temperatures for further studies were selected based on thermogravimetric analysis (Figure 2). The first weight loss was observed around 200°C (P1), the second at about 400°C (P2), the third at 600°C (P3) and the end at about 800°C (P4).

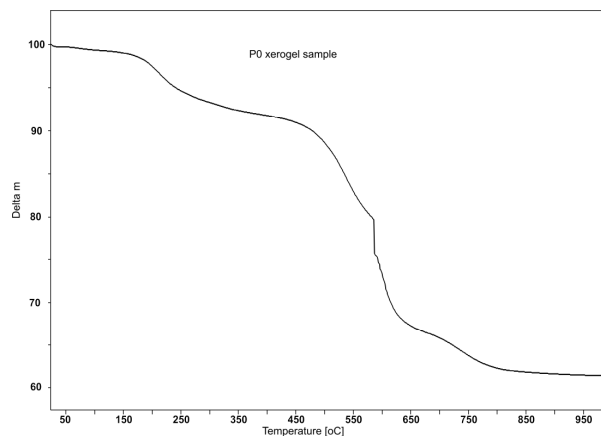


Figure 2. Thermogravimetric (TG) curve of P0 sample

Spectroscopic studies (MIR and Raman) of samples (P0-P4) show that the transition from xerogel into black glasses (Figures 3 and 4). On MIR spectrum of P1, an increase in intensity of bands responsible for C-H vibrations ( $857, 1270, 1409, 2910, 2969 \text{ cm}^{-1}$ ) and the appearance of additional bands in the range of approx.  $3055 \text{ cm}^{-1}$  (vibration  $CH \text{ sp}^2$ ) and OH at  $3693, 3756 \text{ cm}^{-1}$  is observed. This is most probably due to formation of D-oligomers [1]. As temperature increases (P2 - P4) a decrease in the intensity of the bands associated with the CH groups can be observed [10].

